Thermodynamic and electronic properties of rutile $Sn_{1-x}Ge_xO_2$ alloys from first principles

Yann L. Müller [1,2,*] Alp Umut Kurbay [3,*] Xiao Zhang [3] Emmanouil Kioupakis [3,†] and Anirudh Raju Natarajan [1,2,‡]

[1] *Laboratory of Materials Design and Simulation (MADES), Institute of Materials, École Polytechnique Fédérale de Lausanne, Lausanne, Switzerland*

[2] *National Centre for Computational Design and Discovery of Novel Materials (MARVEL), École Polytechnique Fédérale de Lausanne, Lausanne, Switzerland*

[3] *Department of Materials Science and Engineering, University of Michigan, Ann Arbor, Michigan 48109, USA*

(Received 27 January 2026; accepted 17 June 2026; published 27 July 2026)

Rutile $Sn_{1-x}Ge_xO_2$ alloys are promising materials for high-power electronic applications due to their dopability and tunable ultrawide band gaps. We use first-principles density functional theory and statistical mechanics to investigate the crystallographic, electronic, and thermodynamic properties of rutile $Sn_{1-x}Ge_xO_2$ alloys. We predict that the lattice parameters follow Vegard's law, while band gaps calculated with the hybrid HSE06 functional exhibit strong bowing, consistent with experiment. We also predict that the disordered phase has a large positive mixing enthalpy and a slight tendency for Ge-Sn clustering, indicated by weakly negative short-range order parameters. This large positive mixing enthalpy produces a miscibility gap with a critical temperature above 2300 K, implying that the high Ge and Sn solubilities observed in thin-film synthesis cannot be explained by the incoherent phase diagram alone. We demonstrate that coherency strain substantially alters phase stability. Calculations of the coherent spinodal show significant suppression of the miscibility gap, reducing the critical temperature to ≈ 900 K. These coherent phase boundaries could account for the experimentally observed high solubilities at typical growth temperatures. Our results indicate that coherency strain stabilizes these metastable alloys and enables band-gap engineering in this ultrawide-band-gap material system.

DOI: 10.1103/q3ht-wjty

I. INTRODUCTION

Semiconductors with band gaps wider than that of GaN (3.4 eV), known as ultrawide-band-gap (UWBG) semiconductors, are promising for high-power electronic devices and UV-visible optoelectronics [1]. UWBG materials can tolerate higher electric fields than conventional semiconductors due to the superlinear increase of the critical dielectric breakdown field with increasing band gap. Several UWBG materials are under investigation [1], including diamond, cubic boron nitride, aluminum-gallium-nitride alloys, and semiconducting oxides such as β–Ga_2O_3, SnO_2, rutile GeO_2, and rutile SiO_2 [2,3].

Rutile GeO_2 (r-GeO_2) and its alloys with SnO_2, in particular, have recently emerged as promising materials for UWBG applications due to their attractive electronic properties. r-GeO_2 has been predicted to exhibit an ultrawide band gap of 4.68 eV [4], efficient n-type (and potential ambipolar) doping [5], high electron and hole mobilities [6], and high thermal conductivity [7]. The large band gap and high carrier mobilities of r-GeO_2 yield a high Baliga's figure of merit [8] surpassing other power electronic candidates such as Ga_2O_3. The n-type dopability has been experimentally demonstrated for bulk [9] and thin-film [10] samples, while MOSFET devices [11] and vertical Schottky barrier diodes [12] based on r-GeO_2 have recently been demonstrated.

Alloying r-GeO_2 with r-SnO_2 yields a tunable band gap ranging from 4.68 eV (r-GeO_2) to 3.6 eV (r-SnO_2). Pulsed laser deposition [13,14], chemical vapor deposition [15], sputtering [16,17], and molecular beam epitaxy [18,19] have been utilized to synthesize rutile $Sn_{1-x}Ge_xO_2$ (r-$Sn_{1-x}Ge_xO_2$). However, film quality is sensitive to the composition, often suffering from amorphization and challenges in obtaining single-phase films as the Ge content increases.

In this study, we systematically investigate the thermodynamic and electronic properties of r-$Sn_{1-x}Ge_xO_2$ alloys using density functional theory (DFT) and statistical mechanics-based calculations. Our results reveal that the lattice parameters of disordered solid solutions follow Vegard's law, and the band gaps exhibit a bowing effect. Finite-temperature thermodynamic calculations, based on both an approximate free-energy model and more accurate Monte Carlo simulations informed by on-lattice cluster expansions, predict a high-temperature miscibility gap consistent with early experiments. Finally, we show that the variation in solid solubilities observed across synthesis techniques likely stems from the suppression of the miscibility gap due to coherency strain. Our results highlight the importance of accounting for coherency strain effects on phase stability in alloys of r-GeO_2.

II. METHODS

Density functional theory (DFT) calculations with the Perdew-Burke-Ernzerhof (PBE) [20], r^{2}SCAN [21], and

*These authors contributed equally to this work.
†Contact author: kioup@umich.edu
‡Contact author: anirudh.natarajan@epfl.ch

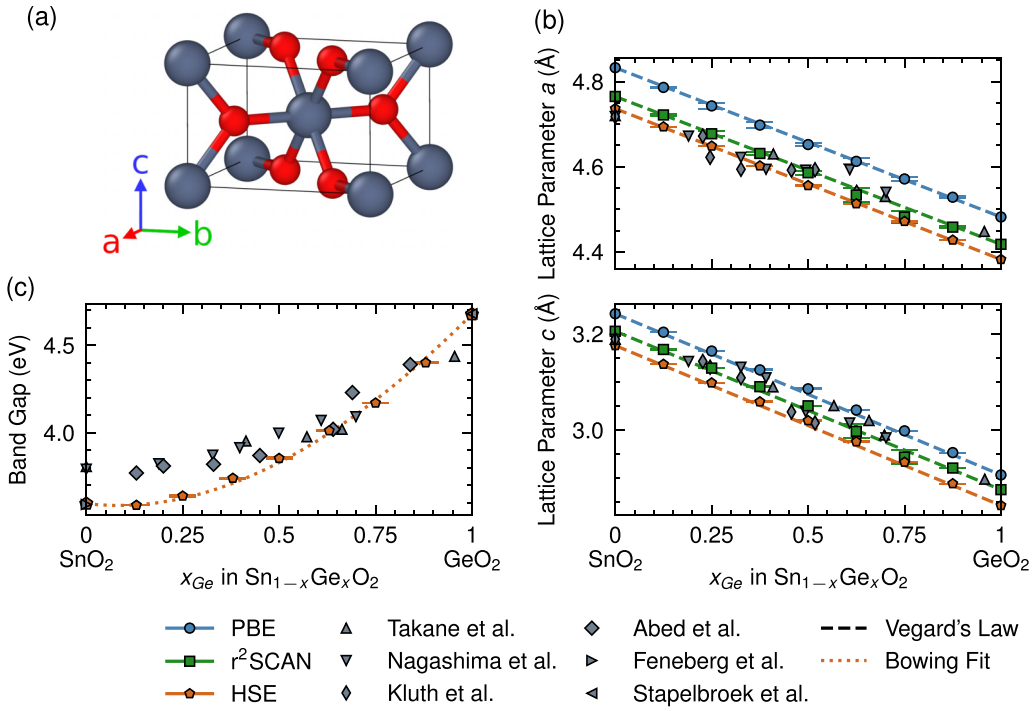

FIG. 1. (a) Unit cell of the rutile structure. The blue atoms correspond to cation sites occupied by Ge or Sn atoms, while red sites correspond to oxygen atoms. (b) Calculated PBE (blue circles), r^{2}SCAN (green squares), HSE (orange pentagons) lattice constants a (top) and c (bottom), for $Sn_{1-x}Ge_xO_2$ alloys at $x = 0$, 0.125, 0.25, 0.375, 0.5, 0.625, 0.75, 0.875, 1. The values for the alloys are calculated by averaging three SQS supercells, each containing 72 atoms (a $2 \times 2 \times 3$ supercell of the primitive unit cell). The error bars represent the standard deviation. (c) Calculated HSE band gaps (orange pentagons) for $Sn_{1-x}Ge_xO_2$ alloys using 72 atom SQSs. The bowing fit is determined using a second-order composition-dependent model. The experimental data for alloy thin films are given by [15] (upward triangles), [13] (downward triangles), [17] (diamonds), and [14] (rhombuses), while the data for the bulk crystals is given by [26] (rightward triangles) and [27] (leftward triangles).

HSE06 [22] functionals were used to study the crystallographic, thermodynamic, and electronic properties of r-$Sn_{1-x}Ge_xO_2$. We employed HSE06 hybrid-functional calculations, in particular, to obtain accurate band gaps, as the other two functionals systematically underestimate them. All performed DFT calculations were non-spin-polarized and used projector augmented-wave (PAW) potentials as implemented in the Vienna *ab initio* Simulation Package (VASP) [23,24]. We relaxed structures with the PBE [20] and r^{2}SCAN functionals until forces on atoms converged to less than 0.01 eV/Å. These calculations treated Ge $4s^2 3d^{10} 4p^2$ and Sn $5s^2 4d^{10} 5p^2$ as valence electrons, with a plane-wave energy cutoff of 600 eV and a Γ-centered k-point mesh with a reciprocal-space density of 35 Å^{-1}. For the HSE calculations, we used GW-compatible PBE pseudopotentials and the screened hybrid HSE06 functional with a modified short-range Hartree-Fock exact exchange fraction of α=0.315 for all compositions. This value was chosen to reproduce the experimental band gaps of the terminal oxides, as detailed in Appendix A. The HSE06 calculations included the Ge $3s^2\ 3p^6$ and Sn $4s^2\ 4p^6$ electrons in addition to those above, which necessitated an increased plane-wave energy cutoff of 950 eV to ensure total energy convergence within 1 meV/atom. We sampled the Brillouin zone with a Γ-centered $4 \times 4 \times 6$ grid for binary unit cells and a Γ-centered $2 \times 2 \times 2$ grid for alloy supercells.

The cation sublattice of the rutile parent structure, shown in Fig. 1(a), can be occupied by either Ge or Sn atoms, allowing for chemical disorder in the $Sn_{1-x}Ge_xO_2$ alloy. We do not consider disorder on the anion (oxygen) sublattice. We approximate properties of the disordered phase using special quasirandom structures (SQS) [25]. SQS-based chemical orderings were generated in a simulation cell containing 72 atoms (24 formula units) for seven equally spaced compositions ranging from pure SnO_2 ($x = 0$) to GeO_2 ($x = 1$), ensuring that pair cluster functions were disordered up to the sixth nearest-neighbor shell. We relaxed structures with respect to lattice parameters and atomic positions using the PBE, r^{2}SCAN, and HSE06 functionals to obtain lattice parameters and total energies. The band gaps of the SQS structures were calculated with the HSE06 functional.

Understanding the finite-temperature synthesizability of disordered r-$Sn_{1-x}Ge_xO_2$ alloys requires quantifying the thermodynamics of the binary alloy. Finite-temperature free energies can be estimated through several methods. The simplest approximation uses the energies of SQS structures to construct a free energy model. The formation energy (Δe_f) for a specific arrangement of Ge and Sn on the rutile lattice is given by

$$\Delta e_f(Sn_{2(1-x)}Ge_{2x}O_4) = \frac{2}{M}(E(Sn_{(M-N)}Ge_NO_{2M}) - NE(GeO_2) - (M-N)E(SnO_2)), \quad (1)$$

where $E(Sn_{(M-N)}Ge_NO_{2M})$ is the total energy of a supercell containing M total cation sites. N of these sites are occupied by Ge (giving a composition $x = N/M$). $E(GeO_2)$

and $E(SnO_2)$ are the total energies per formula unit of bulk rutile GeO_2 and SnO_2, respectively. Equation (1) is the formation energy per rutile primitive cell containing two formula units of r-$Sn_{1-x}Ge_xO_2$. The formation energies of the SQS structures are used to approximate the mixing enthalpy (Δh_{dis}) of the disordered solid solution with a subregular solution model

$$\Delta h_{\text{dis}}(Sn_{2(1-x)}Ge_{2x}O_4) = \alpha_h x(1-x) + \beta_h x(1-x)(1-2x), \tag{2}$$

where α_h and β_h are parameters fit to the DFT-computed SQS formation energies. The ideal mixing entropy (Δs_{dis}) per primitive cell is estimated as

$$\Delta s_{\text{dis}}(Sn_{2(1-x)}Ge_{2x}O_4) = -2k_B(x\ln(x) + (1-x)\ln(1-x)), \tag{3}$$

where the factor of 2 arises from the two cation sites within the rutile primitive unit cell. The free energy of the disordered phase is computed as $\Delta g_{\text{disordered}}(Sn_{2(1-x)}Ge_{2x}O_4, T) = \Delta h_{\text{dis}} - T\Delta s_{\text{dis}}$.

An open question is whether oxygen vacancies influence the thermodynamic stability of $Sn_{1-x}Ge_xO_2$ alloys. Prior first-principles calculations indicate that oxygen vacancies preferentially adopt the neutral charge state under n-type conditions, with formation energies $E_{\text{form}}(V_O)$ of at least ~1.5 eV in SnO_2 [28] and ~2.2 eV in GeO_2 [5] under O-poor growth conditions. At typical growth temperatures of 1000 K, and using the Boltzmann distribution $\exp(-E_{\text{form}}(V_O)/k_BT)$, we estimate a probability of 2×10^{-8} for an oxygen site to be vacant, which corresponds to an equilibrium oxygen vacancy concentration on the order of 10^{15} cm^{-3}. Such low vacancy densities are unlikely to play a significant role in thermodynamic stability of $Sn_{1-x}Ge_xO_2$ alloys.

The approximate free energy model constructed with the formation energies of the SQS structures and ideal solution mixing entropy does not account for the formation of any ordered phases or the formation of short-range order within the disordered solid solution. A more accurate estimate of finite-temperature thermodynamics in systems with order-disorder transitions can be obtained from statistical mechanics simulations. These simulations are informed by surrogate models, such as on-lattice cluster expansions (CE), which are parameterized using DFT calculations for a small set of symmetrically distinct arrangements on a parent crystal structure. Cluster expansion Hamiltonians [29,30] are effective tools for assessing the thermodynamic properties of crystalline materials [31–41]. Within the cluster expansion formalism, any arrangement of Sn and Ge on the rutile lattice is represented by an occupation vector $\vec{\sigma} = [\sigma_1\ \sigma_2\ \ldots\ \sigma_N]^T$. The ith entry σ_i takes the value 1 if the ith lattice site is occupied by Sn and -1 if occupied by Ge. The formation energy $\Delta e_f(\vec{\sigma})$ of an arbitrary arrangement $\vec{\sigma}$ in this alloy is given by:

$$\Delta e_f(\vec{\sigma}) = \frac{1}{M}\left(V_0 + \sum_i V_i\sigma_i + \sum_{i,j} V_{ij}\sigma_i\sigma_j + \ldots\right), \tag{4}$$

where V_0, V_i, and V_{ij} are fitting coefficients known as effective cluster interactions (ECI). The CE is then used within Monte Carlo simulations and free-energy integration methods to compute the finite-temperature free energy of all relevant phases in the alloy. Common tangent constructions are then employed to compute phase boundaries.

III. RESULTS

Figure 1 shows the calculated lattice constants and band gap of r-$Sn_{1-x}Ge_xO_2$ alloys as a function of alloy composition x. Figure 1(b) shows the calculated PBE, r^{2}SCAN, and HSE lattice constants averaged over three SQS supercells containing 72 atoms. The HSE and r^{2}SCAN results are in excellent agreement with experimental studies, whereas PBE overestimates the lattice constants due to the well-known underbinding tendency of the functional. The calculated lattice constants clearly demonstrate the validity of Vegard's law in all three cases.

The band gaps for the SQS structures computed with the HSE06 hybrid functional are shown in Fig. 1(c). Band gaps are averaged over three different SQSs at each composition. The calculated fundamental band gaps of r-GeO_2 and r-SnO_2 are 4.67 eV and 3.62 eV, respectively. We find a direct band gap at the Γ point across all compositions, which is fit to a second-order composition-dependent bowing model:

$$E_g(x) = xE_{g,\text{Ge}} + (1-x)E_{g,\text{Sn}} - [\alpha_g x(1-x) + \beta_g x(1-x)(1-2x)]. \tag{5}$$

The second-order bowing fit is employed here to more effectively capture composition-dependent variations in the bowing behavior, as observed in other UWBG semiconductor alloys such as $Al_{1-x}In_xN$ [42]. This fit yields bowing parameters $\alpha_g = 1.23 \pm 0.04$ eV and $\beta_g = 0.11 \pm 0.06$ eV, where α_g corresponds to the bowing magnitude and β_g describes the bowing asymmetry. In the second-order fit, the symmetric bowing parameter $\alpha_g = 1.23$ eV is comparable in magnitude to the first-order bowing parameter reported experimentally by Takane *et al.*, who obtained $b = 1.2$ eV [15]. The positive value of β_g indicates that r-$Sn_{1-x}Ge_xO_2$ alloys exhibit stronger band gap bowing at lower Ge content. While our calculated band gap of 3.62 eV for SnO_2 agrees with experimental studies of the bulk material, this value is roughly 200 meV lower than that reported in experimental optical absorption measurements for thin-film samples [13,15]. This discrepancy may arise from the dipole-allowed or dipole-forbidden nature of the optical transitions, which can depend on symmetry breaking induced by alloy disorder. Additionally, substrate-induced strain in thin-film samples may modify the band gap due to the large deformation potentials of these materials [43,44].

Figure 2 compares the 0 K and finite-temperature phase stability of r-$Sn_{1-x}Ge_xO_2$ alloys as computed with different exchange-correlation functionals. The formation energies of the 21 SQS orderings, shown in Fig. 2(a), are qualitatively similar when computed with PBE and r^{2}SCAN. However, the r^{2}SCAN values are up to 17% higher than the PBE values, a difference that is largest at high germanium compositions. Both DFT functionals predict positive mixing enthalpies. This result indicates low-temperature phase separation and suggests that mixing between the terminal oxides occurs only at higher temperatures. We used the SQS formation energies of Fig. 2(a) to fit the subregular solution model for the disordered phase enthalpy [Eq. (2)]. The resulting fitting

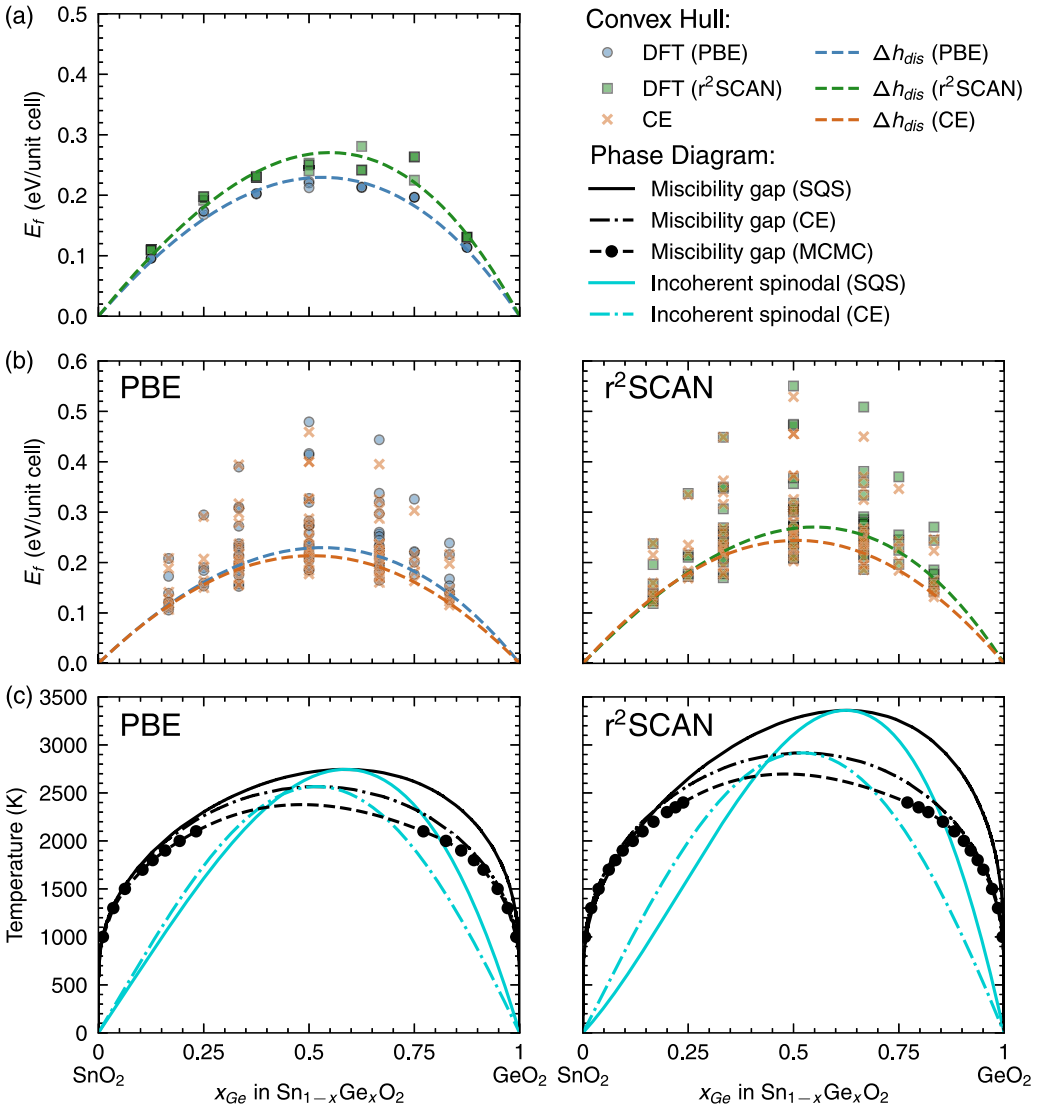

FIG. 2. (a) DFT formation energies of the SQS structures evaluated with PBE (blue circles) and r^{2}SCAN (green squares) functionals. The dashed lines represent the enthalpy of the disordered phase estimated with the subregular solution model. (b) Convex hull computed with 80 symmetrically distinct orderings on r-Sn$_{1-x}$Ge$_x$O$_2$ predicted by DFT (blue circles) and CE (orange crosses), computed using PBE functional (left) and r^{2}SCAN functional (right). The blue dashed lines are the disordered enthalpy estimated with the subregular solution model fit to the DFT formation energies of the SQS structures. The orange dashed line is the enthalpy of a perfectly disordered solid solution estimated with the CE model. (c) Phase diagrams of the r-Sn$_{1-x}$Ge$_x$O$_2$ computed using PBE functional (left) and r^{2}SCAN functional (right). The black solid line indicates the miscibility gap and the turquoise line the incoherent spinodal. The miscibility gap obtained through free energy integration using the CE is indicated by black dots.

parameters are listed in Table I. The large positive values of α_h in Table I indicate significant immiscibility in this alloy. The SQS-based approximate free energy model generally provides finite-temperature predictions consistent with experiment, but quantitative differences in phase stability can arise from short- or long-range ordering effects. A rigorous evaluation of finite-temperature phase stability was performed using the CE method. We computed the formation energies of all 80 symmetrically distinct chemical decorations of Ge and Sn on the rutile cation sublattice within supercells containing up to six cation sites using both PBE and r^{2}SCAN functionals. The computed formation energies are shown in Fig. 2(b). No ordered ground states are predicted to be stable at 0 K. The positive formation energies suggest immiscibility at low temperatures, in agreement with the formation energies of the SQS orderings in Fig. 2(a). To parametrize the CE model based on these 80 formation energies, descriptors of chemical ordering were computed with the Clusters Approach to Statistical Mechanics (CASM) software package [45–47] for

TABLE I. Fitting parameters for the subregular solution model of the disordered phase enthalpy, based on Eq. (2).

	α_h (eV/unit cell)	β_h (eV/unit cell)
Δh_{dis} (PBE)	0.915	–0.117
Δh_{dis} (r^{2}SCAN)	1.071	–0.219

clusters containing up to four sites located within a maximum distance of 9 Å. A fivefold cross-validated Lasso model [48], as implemented in the SKLEARN package [49], was utilized for the linear regression. The resulting CE models achieved a training root mean-squared error (RMSE) of 9 meV/unit cell (1.5 meV/atom) and 11 meV/unit cell (1.8 meV/atom), for PBE and r^{2}SCAN functionals, respectively. In particular, the average fivefold cross-validation error is 23 meV/unit cell (27 meV/unit cell) achieved for an optimum regularization strength of 0.00034 (0.00039) for the PBE (r^{2}SCAN) functional. A comparison between the DFT and CE formation energies is shown in Fig. 2(b).

Figure 2(c) shows the finite-temperature phase diagrams computed with the PBE and r^{2}SCAN functionals, for three different free energy models. In the case of the SQS-based free energy model, both phase diagrams predict a wide miscibility gap, indicating phase separation. For an equiatomic solid solution, the critical temperature is predicted to be ∼2750 K with PBE and ∼3350 K with r^{2}SCAN. The higher critical temperature from r^{2}SCAN is a direct result of the larger SQS formation energies predicted by that functional. These results are in qualitative agreement with the experimental phase diagram reported by Watanabe *et al.* [50]. Their work suggests ≈4% solubility of GeO_2 in SnO_2 at 1250 °C, with very little solubility of SnO_2 in GeO_2. Our calculations show a similar trend, predicting low solubility of GeO_2 in SnO_2 and minimal dissolution at the GeO_2-rich end of the phase diagram. Vibrational entropy is not included in the free energies of Fig. 2. While its omission may shift the predicted order-disorder transition temperatures quantitatively, it is unlikely to alter the qualitative trends.

Figure 2(b) compares the mixing enthalpies estimated directly from the CE against the approximate values fit to the SQS formation energies. The CE mixing enthalpy is approximately 7% lower than the SQS-based PBE value, which alone accounts for a ≈100 K reduction in the predicted critical temperature [Fig. 2(c)]. Figure 2(c) also shows the phase diagram from finite-temperature Monte Carlo simulations, followed by free energy integration and common tangent construction, which account for short-range order in the disordered solid solutions. These simulations, shown by the dashed line in Fig. 2(c), yield a miscibility gap with a critical temperature nearly 400 K lower than that predicted by the SQS-based free energy model.

The lower critical temperature from Monte Carlo simulations, relative to the CE-based mean-field prediction, arises from short-range order (SRO) near the phase transition. SRO reduces both the mixing enthalpy and the configurational entropy of the disordered state compared to a perfectly random solution. When the enthalpy reduction exceeds the entropy penalty, the free energy of the disordered state decreases. Figure 3 displays the SRO of Ge-Sn pairs in the first, second, and third nearest-neighbor shells from Monte Carlo simulations at 2400 K, just above the predicted critical temperature, and at 3000 K, well above it, using the PBE-parameterized CE. A negative SRO parameter indicates more Ge-Sn pairs than in a random alloy, while a positive value indicates fewer. The data reveal a slight tendency for Ge-Sn clustering in the first nearest-neighbor shell [vertical edges in Fig. 1(a)], while Ge-Ge and Sn-Sn pairs are more prevalent in the second and third nearest-neighbor shells. The absolute SRO values remain below 0.15, and SRO becomes more positive at lower temperatures, consistent with phase-separating behavior. The emergence of SRO near the phase transition accounts for the lower critical temperature predicted by the CE method combined with Monte Carlo simulations relative to the approximate free energy models. Taken together, the results in Fig. 2 indicate a critical temperature of ≈2350–2750 K (PBE) or ≈2700–3350 K (r^{2}SCAN).

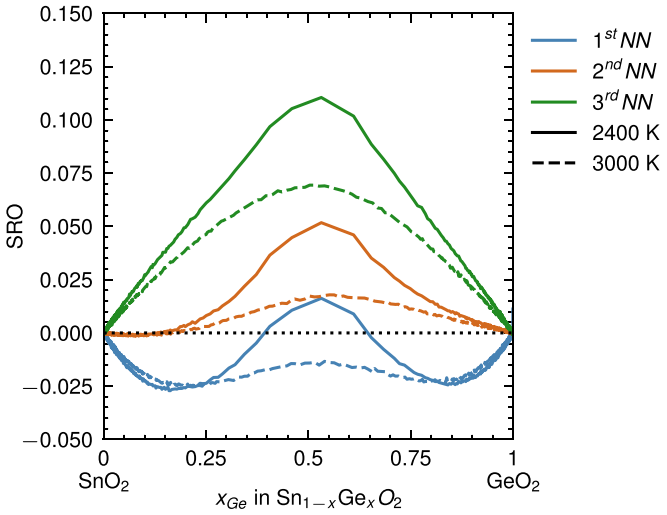

FIG. 3. Plot of the Ge-Sn SRO as a function of the composition for the first (blue), second (orange), and third (green) nearest-neighbor shells, computed at 2400 K (solid line) and at 3000 K (dashed line).

IV. DISCUSSION

The finite-temperature phase diagrams of Fig. 2 agree well with early experiments for bulk materials [50]. However, they appear to contradict recent reports of wide-ranging miscibility in thin films [15,19] and a recent computational prediction [19]. On the computational side, the critical temperature predicted by our thermodynamic model is approximately three times higher than the calculated value of ≈ 986 K reported by Liu *et al.* [19]. This discrepancy exists despite the use of identical DFT functionals in both studies. The difference likely stems from the mixing enthalpy reported by Liu *et al.* [19], which is three times lower than our calculated values (Table I). Liu *et al.* attribute their ability to grow films with 34% Ge in SnO_2 at 600 °C to the metastable solubility limit predicted by their calculated spinodal. In contrast, the spinodal predicted by our models (shown by the turquoise curves in Fig. 2) indicates a metastable solubility limit of only ≈10% at 600 °C. The observed higher solubility of Ge in SnO_2 is unlikely to be explained solely by the incoherent spinodal decomposition and miscibility gap shown in Fig. 2.

The phase diagrams in Fig. 2 represent incoherent equilibria, showing phase boundaries and solubility limits for phases that form without microstructural constraints. Coherency strain can arise internally from the phase separation of the solid solution into a Sn-rich and a Ge-rich phase, which are forced to share a common in-plane lattice parameter at their

coherent interface. As shown in Fig. 1(b), these two phases have distinct equilibrium lattice parameters. The magnitude of the coherency strain is set by their difference. For instance, it can reach up to ∼10% along (001). The coherency strain energy differs from the epitaxial strain, which is imposed by a specific substrate. Coherent phase diagrams differ quantitatively from their incoherent counterparts. This coherency can significantly alter solubility limits and phase stability in materials classes ranging from metallic alloys [51] to thermoelectric [52] and battery materials [53].

Precisely estimating coherent phase equilibrium is challenging as phase compositions are sensitive to microstructure, local stresses, growth conditions, and composition-dependent material properties. Qualitative estimates, however, can be obtained using approximations introduced by Cahn [54] and implemented by Doak and Wolverton [52]. Within this framework, the enthalpy of the disordered phase under the constraint of coherent equilibrium is

$$\Delta h_{\text{dis}}^{\text{coh}}(x) = \Delta h_{\text{dis}}(x) - \Delta e_{\text{cs}}(x), \tag{6}$$

where Δh_{dis} is the incoherent enthalpy of the disordered state [Eq. (2)] and Δe_{cs} is the coherency strain energy due to phase coexistence at the same lattice parameters. As described by Doak and Wolverton [52], an approximate coherency strain energy can be computed along different coexistence planes. This calculation involves fixing the in-plane lattice parameters of the terminal oxides and minimizing the energy with respect to the out-of-plane lattice parameter. The total coherency strain energy for coexistence is the composition-weighted sum of the strain energies of the terminal oxides. The coherency strain energy used in Eq. (6) is the minimum value of this composition-weighted energy found across all possible coexistence directions.

The coherent spinodal, which marks the metastable solubility limit, is the locus of points where the second derivative of the coherent free energy $\Delta g_{\text{dis}}^{\text{coh}} = \Delta h_{\text{dis}}^{\text{coh}}(x) - T\Delta s_{\text{dis}}(x)$ is zero, with ideal solution entropy used for $\Delta s_{\text{dis}}(x)$. The coherency strain energy Δe_{cs} is obtained from a subregular solution model. The model is fitted to the energies estimated with DFT. The CE is utilized to obtain the incoherent enthalpy of the disordered state $\Delta h_{\text{dis}}(x)$. The disordered enthalpy as predicted by the CE is preferred over the SQS-based enthalpy, as it is expected to yield more accurate results. The coherent spinodals are then computed analytically.

Figure 4 shows the effect of coherency strain on the phase stability of r-$Sn_{1-x}Ge_xO_2$. Figure 4(a) shows the coherency strain energies Δe_{cs} computed assuming coexistence along the (001), (100), and (101) planes. The corresponding model parameters are listed in Table II. Coexistence along (001) yields the lowest coherency strain energy, and in the absence of external constraints, coherent interfaces during decomposition are expected to form preferentially along this direction. The coherent mixing enthalpies $\Delta h_{\text{dis}}^{\text{coh}}$ along the (001), (100), and (101) planes are shown in Fig. 4(b). When the coherency strain energy exceeds the incoherent mixing enthalpy, $\Delta h_{\text{dis}}^{\text{coh}}(x)$ becomes negative across the full composition range, implying complete miscibility. This occurs along (100) and (101), where the coherency strain cost fully suppresses the miscibility gap. In practice, coherency along these directions may not be experimentally realized, as the system can lower its free energy by decomposing along elastically softer directions or by forming interfacial defects that relieve the strain.

TABLE II. Fitting parameters for the subregular solution model of the coherency strain energy, based on Eq. (2).

	α_h (eV/unit cell)	β_h (eV/unit cell)
$\Delta e_{\text{cs}}^{001}$ (PBE)	0.601	–0.144
$\Delta e_{\text{cs}}^{001}$ (r^{2}SCAN)	0.801	–0.144
$\Delta e_{\text{cs}}^{100}$ (PBE)	1.176	–0.001
$\Delta e_{\text{cs}}^{100}$ (r^{2}SCAN)	1.331	0.027
$\Delta e_{\text{cs}}^{101}$ (PBE)	1.833	–0.361
$\Delta e_{\text{cs}}^{101}$ (r^{2}SCAN)	2.108	–0.391

The coherent spinodals computed assuming coexistence along the (001) plane are shown in Fig. 4(c), alongside the CE-based miscibility gap and incoherent spinodal. The resulting coherent spinodal, shown by the red lines in Fig. 4(c), is significantly suppressed compared to the incoherent spinodal. The coherent spinodal predicted with PBE reaches a maximum temperature of 980 K at ≈ 35% Ge; the r^{2}SCAN prediction reaches 780 K at ≈ 33% Ge. Despite the more positive incoherent mixing enthalpies predicted by r^{2}SCAN, the coherent spinodal temperatures from both functionals are similar, as the stiffer elastic constants predicted by r^{2}SCAN increase the coherency strain energy and partially offset the higher mixing enthalpy. The asymmetry of the coherent spinodals arises from the asymmetric coherency strain energy: since GeO_2 is stiffer than SnO_2, the coherency strain cost is higher on the Ge-rich side.

The metastable solubility limits predicted by the coherent spinodals in Fig. 4 align well with recent experimental efforts to synthesize r-$Sn_{1-x}Ge_xO_2$. For instance, both the PBE and r^{2}SCAN spinodals predict a coherent Ge solubility limit near $x \approx 0.3$ at temperatures of ≈ 900 K and ≈ 700 K, respectively, consistent with the experimental observations of Liu *et al.* [19]. In the experiments by Takane *et al.* [15], a higher growth temperature of 725 °C was used. At this temperature, our calculations predict nearly complete solid solubility across the entire composition space, consistent with their synthesis of alloys across the full composition range.

Our computational predictions for the crystallographic parameters and finite-temperature thermodynamics of r-$Sn_{1-x}Ge_xO_2$ show qualitative agreement with experiments [15,19]. The coherent spinodals predicted in Fig. 2 assume that entropy arises solely from configurational disorder, that the coherency strain energy can be approximated from the strain energies of the pure phases, and that the lattice is defect free. More rigorous estimates would require advanced techniques such as machine-learned interatomic potentials or CE models that couple ordering and strain degrees of freedom [55]. Such atomistic models would enable rigorous treatment of vibrational contributions, coherency strain energies, and defects such as dislocations or semicoherent interfaces, which have been shown to affect coherent phase separation [56–58]. Furthermore, during thin-film growth, the substrate dictates both the film orientation and its in-plane lattice parameter. The epitaxial constraints imposed by the substrate on the thin

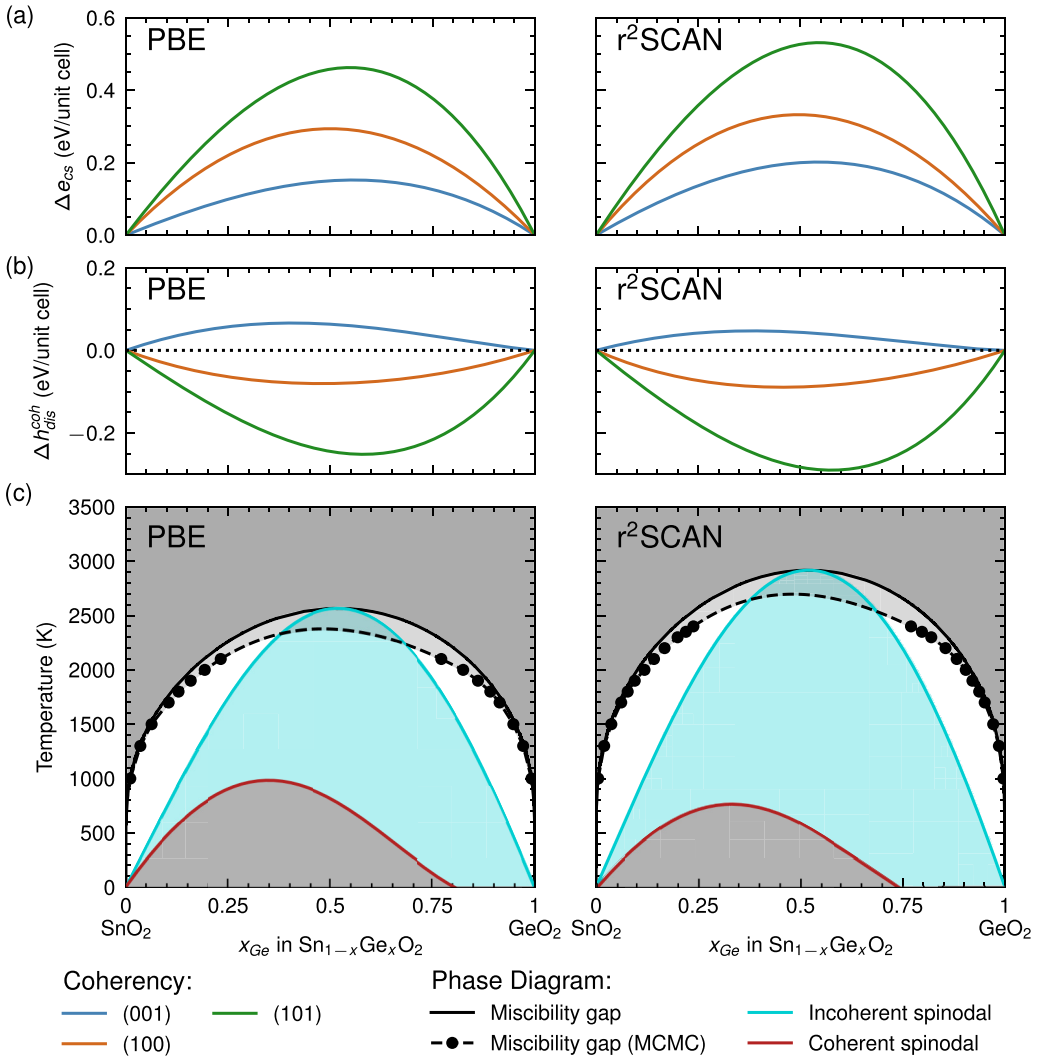

FIG. 4. (a) Coherency strain energies $\Delta e_{\rm cs}$ and (b) enthalpies of the disordered phase under the constraint of coherent equilibrium $\Delta h_{\rm dis}^{\rm coh}$ as a function of the composition between SnO_2 and GeO_2, from the PBE functional (left) and r^{2}SCAN functional (right). Coherent interfaces lie along the (001) (blue), (101) (orange), and (100) (green) planes. (c) Phase diagrams of r $-$ $Sn_{1-x}Ge_xO_2$ from the PBE functional (left) and r^{2}SCAN functional (right). The solid black line marks the miscibility gap, the turquoise line the incoherent spinodal, and the red line the coherent spinodal along the (001) plane. The CE model gives the incoherent enthalpy of the disordered state $\Delta h_{\rm dis}$. Black dots show the miscibility gap obtained through free energy integration with the CE.

film are not explicitly included in our calculations, and may shift the coexistence planes and metastability limits. For instance, our estimates suggest that enforcing coexistence along the (100) or (101) planes could produce complete miscibility even at low temperatures due to large coherency strain energies. If growth conditions force coexistence along these high-strain planes, interfacial defects would likely form to reduce the total free energy. Finally, our model does not account for amorphization, which has been observed experimentally. Predicting amorphization would require estimates of the amorphous phase free energy to compare against that of coherent coexistence during synthesis.

V. CONCLUSION

We investigated the crystallographic, electronic, and thermodynamic properties of the rutile $Sn_{1-x}Ge_xO_2$ alloy using density functional theory at varying levels of accuracy. Lattice parameters predicted by the PBE, r^{2}SCAN, and HSE06 functionals agree well with experimental values and follow Vegard's law, consistent with previous reports [15,19]. Band gap calculations using the HSE06 functional reveal strong bowing at low Ge content, also consistent with previous observations [15]. Finite-temperature phase stability calculations indicate a slightly negative SRO parameter for Ge-Sn pairs in the first neighbor shell and show that the incoherent miscibility gap cannot explain the high Ge solubilities observed in recent experiments, as it predicts low solubility at typical synthesis temperatures. Our calculations instead reveal that coherency strain suppresses the miscibility gap, enabling large Ge and Sn solubilities in agreement with experiments. These findings provide guidance for engineering UWBG semiconductors with tunable properties and highlight the role of coherency strain in enabling band gap engineering.

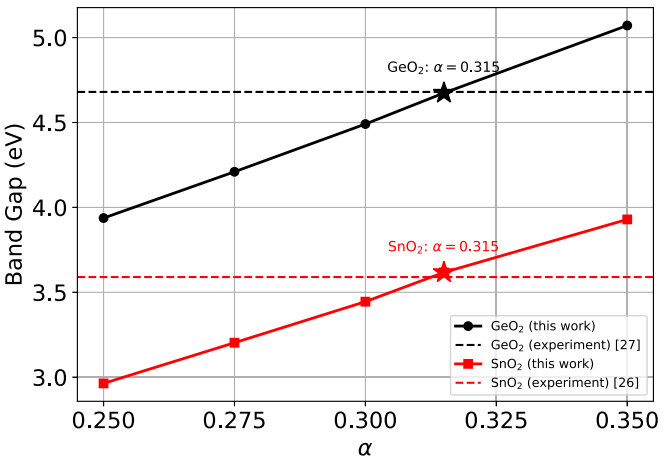

FIG. 5. Calculated HSE band gaps of rutile SnO_2 and GeO_2 as a function of the HSE mixing parameter α. Horizontal dashed lines indicate the experimental band gaps.

ACKNOWLEDGMENTS

Y.L.M. and A.R.N. acknowledge funding from the NCCR MARVEL, a National Centre of Competence in Research supported by the Swiss National Science Foundation (Grant No. 205602), which also provided hospitality and support for E.K.'s sabbatical stay at EPFL, during which part of this work was performed. A.U.K., X.Z., and E.K. were supported by the National Science Foundation through Grant No. 2328701, which is supported in part by federal agency and industry partners through the Future of Semiconductors (FuSe) program. Computational resources were provided by Anvil at Purdue University through allocation DMR200031 from the ACCESS program, supported by U.S. National Science Foundation Grants No. 2138259, No. 2138286, No. 2138307, No. 2137603, and No. 2138296, and by Eiger at the Swiss National Supercomputing Centre (project ID mr30) under the NCCR MARVEL allocation.

DATA AVAILABILITY

The data that support the findings of this article are openly available [59].

TABLE III. Calculated HSE band gaps from this work compared with experimental values for bulk rutile SnO_2 and GeO_2.

Material	HSE Band gap (eV)	Experimental Band gap (eV)
SnO_2	3.617	3.59 ± 0.2 [26]
GeO_2	4.674	4.68 ± 0.002 [27]

APPENDIX A: HSE MIXING PARAMETER CALIBRATION

This Appendix describes the calibration of the HSE06 exact exchange fraction α for the rutile $Sn_{1-x}Ge_xO_2$ alloy system. We calculated the band gaps of the terminal oxides SnO_2 and GeO_2 as a function of α between 0.25 and 0.35 and compared them with experimental band gaps [26,27]. The optimal $\alpha = 0.315$ values for both SnO_2 and GeO_2 were determined from the intersections between the calculated trends and the experimental values, as depicted in Fig. 5. Typically, the composition-dependent mixing parameter for alloys is obtained by linearly interpolating between the optimized end compound values. However, since both end compounds could be modeled accurately with the same mixing parameter, we chose to use $\alpha = 0.315$ across all compositions.

The calculated fundamental gaps of the terminal oxides are compared to bulk experimental results in Table III below.

APPENDIX B: BAND STRUCTURES AND EFFECTIVE MASSES

This Appendix presents additional electronic structure results for rutile SnO_2, $Ge_{0.5}Sn_{0.5}O_2$, and GeO_2. The calculated HSE band structures for rutile GeO_2 and rutile SnO_2 in Fig. 6(a) and 6(c) are consistent with prior theoretical work in the literature [4,60]. The alloy band structure is evaluated for one SQS at x = 0.5 through band unfolding using the vaspkit code [61] and is presented in Fig. 6(b), where darker points correspond to larger spectral weights and therefore greater Bloch character.

The $Ge_{0.5}Sn_{0.5}O_2$ band structure shows that alloying does not significantly alter the location or curvature of the band extrema. Furthermore, we perform a quadratic fit of the points near the band extrema (within 0.3 eV of VBM and 0.8 eV of

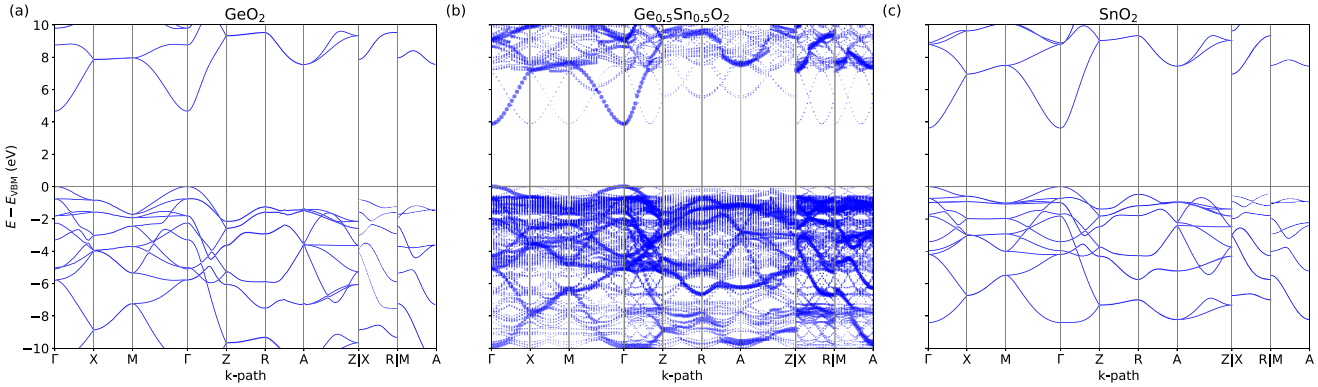

FIG. 6. Calculated HSE band structures of (a) rutile GeO_2, (b) $Ge_{0.5}Sn_{0.5}O_2$, and (c) rutile SnO_2.

TABLE IV. Calculated electron and hole effective masses along the $\Gamma \rightarrow X$ and $\Gamma \rightarrow Z$ directions for rutile SnO_2, $Ge_{0.5}Sn_{0.5}O_2$, and GeO_2, compared with prior theoretical and experimental values where available. Effective masses are reported in units of the free electron mass m_0.

		This Work		Theory Ref.		Experiment Ref.	
Material	Direction	Electron (m_0)	Hole (m_0)	Electron (m_0)	Hole (m_0)	Electron (m_0)	Hole (m_0)
SnO_2	$\Gamma \rightarrow X$	0.32	1.46	0.26–0.309 [60,62]	1.21–1.37 [62,63]	0.299 [64]	–
	$\Gamma \rightarrow Z$	0.28	1.97	0.21–0.211 [60,62]	1.47–1.61 [62,63]	0.234 [64]	–
$Ge_{0.5}Sn_{0.5}O_2$	$\Gamma \rightarrow X$	0.29	1.41	–	–	–	–
	$\Gamma \rightarrow Z$	0.26	1.93	–	–	–	–
GeO_2	$\Gamma \rightarrow X$	0.3	1.16	0.43 [4]	1.28 [5]	–	–
	$\Gamma \rightarrow Z$	0.24	1.73	0.23 [4]	1.74 [5]	–	–

CBM, and 20% of the BZ path) to obtain anisotropic carrier effective masses, as depicted in Table IV. The m^* values for $Ge_{0.5}Sn_{0.5}O_2$ fall intermediate of the two end compounds, which is expected. The results for the end compounds are comparable to values reported in the literature. We attribute any discrepancy with other theoretical studies to the level of theory applied, such as GW corrections, which would modify the band curvature.

[1] M. H. Wong, O. Bierwagen, R. J. Kaplar, and H. Umezawa, Ultrawide-band gap semiconductors: An overview, J. Mater. Res. **36**, 4601 (2021).

[2] J. L. Lyons and A. Janotti, A p-type dopable ultrawide-band gap oxide, J. Phys.: Condens. Matter **36**, 085501 (2024).

[3] S. Chae, N. Sanders, K. A. Mengle, A. Wang, X. Zhang, J. L. Bartolome, K. Luo, Y.-C. Huang, F. Giustino, J. T. Heron, and E. Kioupakis, Extreme-band-gap semiconductors with shallow dopants and mobile carriers, npj Comput Mater (2026)10.1038/s41524-026-02173-z.

[4] K. A. Mengle, S. Chae, and E. Kioupakis, Quasiparticle band structure and optical properties of rutile GeO_2, an ultrawide-band-gap semiconductor, J. Appl. Phys. **126**, 085703 (2019).

[5] S. Chae, J. Lee, K. A. Mengle, J. T. Heron, and E. Kioupakis, Rutile GeO_2: An ultrawide-band-gap semiconductor with ambipolar doping, Appl. Phys. Lett. **114**, 102104 (2019).

[6] K. Bushick, K. A. Mengle, S. Chae, and E. Kioupakis, Electron and hole mobility of rutile GeO_2 from first principles: An ultrawide-band gap semiconductor for power electronics, Appl. Phys. Lett. **117**, 182104 (2020).

[7] S. Chae, K. A. Mengle, R. Lu, A. Olvera, N. Sanders, J. Lee, P. F. P. Poudeu, J. T. Heron, and E. Kioupakis, Thermal conductivity of rutile germanium dioxide, Appl. Phys. Lett. **117**, 102106 (2020).

[8] S. Chae, K. Mengle, K. Bushick, J. Lee, N. Sanders, Z. Deng, Z. Mi, P. F. P. Poudeu, H. Paik, J. T. Heron, and E. Kioupakis, Toward the predictive discovery of ambipolarly dopable ultrawide-band-gap semiconductors: The case of rutile GeO_2, Appl. Phys. Lett. **118**, 260501 (2021).

[9] Z. Galazka, R. Blukis, A. Fiedler, S. B. Anooz, J. Zhang, M. Albrecht, T. Remmele, T. Schulz, D. Klimm, M. Pietsch, A. Kwasniewski, A. Dittmar, S. Ganschow, U. Juda, K. Stolze, M. Suendermann, T. Schroeder, and M. Bickermann, Bulk single crystals and physical properties of rutile GeO_2 for high-power electronics and deep-ultraviolet optoelectronics, Physica Status Solidi (B) **262**, 2400326 (2025).

[10] K. Shimazoe, I. Seike, K. Kanegae, and H. Nishinaka, Enhanced growth temperature window and Sb doping of rutile GeO_2 enabled by graded buffer layers, Jpn. J. Appl. Phys. **64**, 50903 (2025).

[11] K. Tetzner, Z. Galazka, A. Thies, A. Külberg, and O. Hilt, Lateral rutile GeO_2 MOSFET devices on single-crystal r-GeO_2 substrates, IEEE Electron Device Lett. **47**, 566 (2025).

[12] K. Kanegae, K. Shimazoe, I. Seike, and H. Nishinaka, Ni/rutile GeO_2 vertical Schottky barrier diode on Nb-doped TiO_2 substrate using Sb-doped graded $Ge_ysn_{1-y}o_2$ buffer layers, Appl. Phys. Express **18**, 041001 (2025).

[13] Y. Nagashima, M. Fukumoto, M. Tsuchii, Y. Sugisawa, D. Sekiba, T. Hasegawa, and Y. Hirose, Deep ultraviolet transparent electrode: Ta-doped rutile $Sn_{1-x}Ge_xO_2$, Chem. Mater. **34**, 10842 (2022).

[14] E. Kluth, Y. Nagashima, S. Osawa, Y. Hirose, J. Blasing, A. Strittmatter, R. Goldhahn, and M. Feneberg, Blue shift of the absorption onset and band gap bowing in rutile $Ge_xSn_{1-x}O_2$, Appl. Phys. Lett. **125**, 122102 (2024).

[15] H. Takane, Y. Ota, T. Wakamatsu, T. Araki, K. Tanaka, and K. Kaneko, Band-gap engineering of rutile-structured SnO_2-GeO_2-SiO_2 alloy system, Phys. Rev. Mater. **6**, 084604 (2022).

[16] A. M. Abed and R. L. Peterson, Effect of post-deposition annealing on crystal structure of RF magnetron sputtered germanium dioxide thin films, J. Vac. Sci. Technol. A **42**, 063403 (2024).

[17] A. M. Abed and R. L. Peterson, Growth and characterization of rutile-type $Ge_xSn_{1-x}O_2$ alloy thin films via RF magnetron sputtering, APL Mater. **13**, 111115 (2025).

[18] S. Chae, H. Paik, N. M. Vu, E. Kioupakis, and J. T. Heron, Epitaxial stabilization of rutile germanium oxide thin film by molecular beam epitaxy, Appl. Phys. Lett. **117**, 072105 (2020).

[19] F. Liu, N. J. Szymanski, K. Noordhoek, H.-s. Shin, D. Kim, C. J. Bartel, and B. Jalan, Unraveling the growth dynamics of rutile $Sn_{1-x}Ge_xO_2$ using theory and experiment, Nano Lett. **25**, 299 (2025).

[20] J. P. Perdew, K. Burke, and M. Ernzerhof, Generalized gradient approximation made simple, Phys. Rev. Lett. **77**, 3865 (1996).

[21] J. W. Furness, A. D. Kaplan, J. Ning, J. P. Perdew, and J. Sun, Accurate and numerically efficient r^{2}SCAN meta-generalized gradient approximation, J. Phys. Chem. Lett. **1**, 8208 (2020).

[22] J. Heyd, G. E. Scuseria, and M. Ernzerhof, Hybrid functionals based on a screened Coulomb potential, J. Chem. Phys. **118**, 8207 (2003).

[23] G. Kresse and J. Furthmuller, Efficient iterative schemes for *ab initio* total-energy calculations using a plane-wave basis set, Phys. Rev. B **54**, 11169 (1996).

[24] P. E. Blöchl, Projector augmented-wave method, Phys. Rev. B **50**, 17953 (1994).

[25] A. Zunger, S.-H. Wei, L. G. Ferreira, and J. E. Bernard, Special quasirandom structures, Phys. Rev. Lett. **65**, 353 (1990).

[26] M. Feneberg, C. Lidig, K. Lange, R. Goldhahn, M. D. Neumann, N. Esser, O. Bierwagen, M. E. White, M. Y. Tsai, and J. S. Speck, Ordinary and extraordinary dielectric functions of rutile SnO_2 up to 20 eV, Appl. Phys. Lett. **104**, 231106 (2014).

[27] M. Stapelbroek and B. D. Evans, Exciton structure in the U.V. absorption edge of tetragonal GeO_2, Solid State Commun. **25**, 959 (1978).

[28] D. O. Scanlon and G. W. Watson, On the possibility of p-type SnO_2, J. Mater. Chem. **22**, 25236 (2012).

[29] J. M. Sanchez, F. Ducastelle, and D. Gratias, Generalized cluster description of multicomponent systems, Physica A **128**, 334 (1984).

[30] D. D. Fontaine, Cluster approach to order-disorder transformations in alloys, in *Solid State Physics*, edited by H. Ehrenreich and D. Turnbull (Academic Press, New York, 1994), Vol. 47, pp. 33–176.

[31] D. K. Lee, Y. L. Müller, and A. R. Natarajan, Modeling the equilibrium vacancy concentration in multi-principal element alloys from first-principles, Acta Mater. **304**, 121752 (2026).

[32] Y. L. Müller and A. R. Natarajan, First-principles thermodynamics of precipitation in aluminum-containing refractory alloys, Acta Mater. **274**, 119995 (2024).

[33] Y. L. Müller and A. R. Natarajan, Constructing multicomponent cluster expansions with machine-learning and chemical embedding, npj Comput. Mater. **11**, 60 (2025).

[34] A. R. Natarajan and A. Van der Ven, First-principles investigation of phase stability in the Mg-Sc binary alloy, Phys. Rev. B **95**, 214107 (2017).

[35] A. R. Natarajan and A. Van der Ven, Machine-learning the configurational energy of multicomponent crystalline solids, npj Comput. Mater. **4**, 56 (2018).

[36] C. A. Paetsch and A. R. Natarajan, First-principles thermodynamics of hydrogen absorption in binary C15 Laves phases, Chem. Mater. **38**, 683 (2026).

[37] M. Ångqvist, D. O. Lindroth, and P. Erhart, Optimization of the thermoelectric power factor: Coupling between chemical order and transport properties, Chem. Mater. **28**, 6877 (2016).

[38] M. Ångqvist and P. Erhart, Understanding chemical ordering in intermetallic clathrates from atomic scale simulations, Chem. Mater. **29**, 7554 (2017).

[39] J. Brorsson, A. E. C. Palmqvist, and P. Erhart, First-principles study of order–disorder transitions in pseudobinary clathrates, J. Phys. Chem. C **125**, 22817 (2021).

[40] D. K. J. Lee, Z. Deng, G. Sai Gautam, and P. Canepa, Thermodynamics of sodium–lead alloys for negative electrodes from first-principles, Chem. Mater. **36**, 6831 (2024).

[41] Z. Wang, T. P. Mishra, W. Xie, Z. Deng, G. S. Gautam, A. K. Cheetham, and P. Canepa, Kinetic Monte Carlo simulations of sodium ion transport in NaSICON electrodes, ACS Mater. Lett. **5**, 2499 (2023).

[42] S. Schulz, M. A. Caro, C. Coughlan, and E. P. O'Reilly, Composition dependent band gap and band edge bowing in AlInN: A combined theoretical and experimental study, Appl. Phys. Lett. **103**, 242102 (2013).

[43] A. Samanta, M. Jain, and A. K. Singh, Ultra-sensitive pressure dependence of band gap of rutile-GeO_2 revealed by many body perturbation theory, J. Chem. Phys. **143**, 064703 (2015).

[44] P. Borlido, J. Schmidt, H.-C. Wang, S. Botti, and M. A. L. Marques, Computational screening of materials with extreme gap deformation potentials, npj Comput. Mater. **8**, 156 (2022).

[45] B. Puchala, J. C. Thomas, A. R. Natarajan, J. G. Goiri, S. S. Behara, J. L. Kaufman, and A. Van der Ven, CASM — A software package for first-principles based study of multicomponent crystalline solids, Comput. Mater. Sci. **217**, 111897 (2023).

[46] A. Van der Ven, J. Thomas, B. Puchala, and A. Natarajan, First-principles statistical mechanics of multicomponent crystals, Annu. Rev. Mater. Res. **48**, 27 (2018).

[47] B. Puchala and A. Van der Ven, Thermodynamics of the Zr-O system from first-principles calculations, Phys. Rev. B **88**, 094108 (2013).

[48] R. Tibshirani, Regression shrinkage and selection via the Lasso, J. Roy. Stat. Soc. B **58**, 267 (1996).

[49] F. Pedregosa, G. Varoquaux, A. Gramfort, V. Michel, B. Thirion, O. Grisel, M. Blondel, P. Prettenhofer, R. Weiss, V. Dubourg, J. Vanderplas, A. Passos, and D. Cournapeau, Scikit-learn: Machine learning in Python, Journal of Machine Learning Research **12**, 2825 2011.

[50] A. Watanabe, T. Kikuchi, M. Tsutsumi, S. Takenouchi, and K. Uchida, Solid solubility of GeO_2 in SnO_2, J. Am. Ceram. Soc. **66**, c104 (1983).

[51] A. R. Natarajan, E. L. Solomon, B. Puchala, E. A. Marquis, and A. Van der Ven, On the early stages of precipitation in dilute Mg–Nd alloys, Acta Mater. **108**, 367 (2016).

[52] J. W. Doak and C. Wolverton, Coherent and incoherent phase stabilities of thermoelectric rocksalt IV-VI semiconductor alloys, Phys. Rev. B **86**, 144202 (2012).

[53] R. Malik, A. Abdellahi, and G. Ceder, A critical review of the Li insertion mechanisms in $LiFePO_4$ electrodes, J. Electrochem. Soc. **160**, A3179 (2013).

[54] J. W. Cahn, On spinodal decomposition, Acta Metall. **9**, 795 (1961).

[55] S. S. Behara, J. C. Thomas, B. Puchala, and A. Van der Ven, Chemomechanics in alloy phase stability, Phys. Rev. Mater. **8**, 033801 (2024).

[56] F. Léonard and R. C. Desai, Spinodal decomposition and dislocation lines in thin films and bulk materials, Phys. Rev. B **58**, 8277 (1998).

[57] S. Hu and L. Chen, Solute segregation and coherent nucleation and growth near a dislocation—a phase-field model

integrating defect and phase microstructures, Acta Mater. **49**, 463 (2001).

[58] S. Hu and L. Chen, Diffuse-interface modeling of composition evolution in the presence of structural defects, Comput. Mater. Sci. **23**, 270 (2002).

[59] MaterialsCloud repository, https://doi.org/10.24435/materialscloud:e2-xp.

[60] A. Wang, K. Bushick, N. Pant, W. Lee, X. Zhang, J. Leveillee, F. Giustino, S. Poncé, and E. Kioupakis, Electron mobility of SnO_2 from first principles, Appl. Phys. Lett. **124**, 172103 (2024).

[61] V. Wang, N. Xu, J.-C. Liu, G. Tang, and W.-T. Geng, Vaspkit: A user-friendly interface facilitating high-throughput computing and analysis using VASP code, Comput. Phys. Commun. **267**, 108033 (2021).

[62] A. Schleife, J. B. Varley, F. Fuchs, C. Rödl, F. Bechstedt, P. Rinke, A. Janotti, and C. G. Van de Walle, Tin dioxide from first principles: Quasiparticle electronic states and optical properties, Phys. Rev. B **83**, 035116 (2011).

[63] J. B. Varley, A. Janotti, and C. G. Van de Walle, Group-V impurities in SnO_2 from first-principles calculations, Phys. Rev. B **81**, 245216 (2010).

[64] K. J. Button, C. G. Fonstad, and W. Dreybrodt, Determination of the electron masses in stannic oxide by submillimeter cyclotron resonance, Phys. Rev. B **4**, 4539 (1971).